

SCIENCE ADVANCES | RESEARCH ARTICLE





Ultrathin silicon nitride microchip for in situ/operando microscopy with high spatial resolution and spectral visibility

Kunmo Koo^{1,2}, Zhiwei Li^{3,4}, Yukun Liu^{1,4}, Stephanie M. Ribet^{1,4}, Xianbiao Fu⁵, Ying Jia^{1,2}, Xinqi Chen^{1,2}, Gajendra Shekhawat^{1,2}, Paul J. M. Smeets^{1,2}, Roberto dos Reis^{1,2}, Jungjae Park⁶, Jong Min Yuk⁶, Xiaobing Hu^{1,2}*, Vinayak P. Dravid^{1,2,4}*

Utilization of in situ/operando methods with broad beams and localized probes has accelerated our understanding of fluid-surface interactions in recent decades. The closed-cell microchips based on silicon nitride (SiN_x) are widely used as "nanoscale reactors" inside the high-vacuum electron microscopes. However, the field has been stalled by the high background scattering from encapsulation (typically ~100 nanometers) that severely limits the figures of merit for in situ performance. This adverse effect is particularly notorious for gas cell as the sealing membranes dominate the overall scattering, thereby blurring any meaningful signals and limiting the resolution. Herein, we show that by adopting the back-supporting strategy, encapsulating membrane can be reduced substantially, down to ~10 nanometers while maintaining structural resiliency. The systematic gas cell work demonstrates advantages in figures of merit for hitherto the highest spatial resolution and spectral visibility. Furthermore, this strategy can be broadly adopted into other types of microchips, thus having broader impact beyond the in situ/operando fields.

Copyright © 2024 me Authors, some rights reserved; exclusive licensee American Association for the Advancement of Science. No claim to original U.S. Government Works. Distributed under a Creative Commons Attribution NonCommercial License 4.0 (CC BY-NC).

INTRODUCTION

The technological solutions to global challenges, from clean energy generation to environmental remediation, are rooted in the fundamental underpinnings of fluid-surface interactions. The need for mapping spatiotemporal interactions at fluid surfaces is of great value in both fundamental understanding and applied technologies (1), as in gas-phase catalysis with nanoparticles (2–4) or atomic clusters, for example. The ability to monitor and measure, in real-space/time, the atomic-scale details of catalyst nanoparticles, coupled to tracing the molecular signatures of input/reactant gases and products, is the "Holy Grail" in the field. Such an ability to spatiotemporally monitor atomic-scale structural and nanoscale spectral changes promises to open new vistas for design catalysts with improved performance and help establish often-elusive structure-property paradigms.

In situ transmission electron microscopy (TEM) and scanning TEM (STEM) experiments provide immense promise in the ability to study materials at extremely high resolution under realistic environmental conditions (5–9). Nonetheless, these devices have traditionally been limited by the physical hardware needed for these types of experiments. The environmental TEM (E-TEM) experiments rely on two distinct hardware setups. One is the open-cell method, with a dedicated environmental microscope, which creates a pressure gradient within the microscope column using a differential pumping system. The other, more popular and widely deployable, approach is the closed-cell method, where the liquid/gas mediums

¹Department of Materials Science and Engineering, Northwestern University, Evanston, IL 60208, USA. ²The NUANCE Center, Northwestern University, Evanston, IL 60208, USA. ³Department of Chemistry, Northwestern University, Evanston, IL 60208, USA. ⁴Internaional Institute for Nanotechnology, Northwestern University, Evanston, IL 60208, USA. ⁵Department of Physics, Technical University of Denmark, Kongens Lyngby, Denmark. ⁶Department of Materials Science and Engineering, Korea Advanced Institute of Science and Technology, Daejeon, Republic of Korea. *Corresponding author. Email: xbhu@northwestern.edu (X.H.); v-dravid@northwestern.edu (V.P.D.)

are encapsulated in-between two membranes in the specimen rod. To create an isolated nanoreactor, a low-stress SiN_x is widely used as the encapsulating membrane. Compared to several other encapsulating materials, such as graphene (10, 11), silicon oxide (SiO_x) (12), and other transition metal dichalcogenides (13), SiN_x has the following advantages such as ease of manufacturing, reliable physical robustness at several tens of nanometers thickness, and reasonable electron transparency.

For open-cell E-TEM, the spatial resolution is superior to the closed-cell system, but this setup can only be used in a gaseous or vapor condition with pressure as low as ~15 torr, which is far removed from many real-life conditions and thus limits many applications. Meanwhile, the cost of a dedicated environmental microscope is much higher than that of a holder, which can host the nanoreactor with liquid/gas mediums encapsulated into a confined space. Therefore, closed-cell E-TEM based on SiN_x membranes is an ideal tool to address fundamental phenomena and physicochemical processes associated with many industrial applications such as catalysis, gas sensing, hydrogen storage, CO₂ capture, and storage, which involves the charge transport and materials conversion occurring at the solid-gas interface in realistic reaction conditions.

Although the in situ gas cell TEM provides great insights into the materials discovery, in many cases, the adverse electron scattering from the ~100-nm-thick encapsulation severely limits resolution and quantitative analyses. Specifically, the atomic concentration and the scattering cross section for commercial SiN_x membranes (30- to 50-nm thickness for single chip) can be far greater than those of the encapsulated atmospheric pressure gas and internal material of interest (14). Thus, ill effects such as low-resolution/contrast images, poor electron energy-loss spectrum (EELS) quality, and highly blurred electron diffraction (ED) containing extensive diffuse scattering from SiN_x membranes can arise. Beyond the resolution limitations that come from adverse scatterings from thick membranes, there are similar considerations in other advanced techniques such as EELS and emerging four-dimensional (4D)–STEM, especially for

quantitative analysis (15, 16). It is widely accepted that reducing the membranes thickness will be the most effective way to alleviate the adverse scattering and improve figures of merit for microscopy. However, hitherto, it has been extremely challenging to fabricate the ultrathin (UT) membrane that has necessary structural robustness and a large field of view coupled to practical considerations of reproducibility and consistency with high yield of production.

Here, we demonstrate a hybrid encapsulation structure to achieve substantially reduced membrane thickness for the fluidic cell (gas cell, in the present case) TEM (Fig. 1A). By adopting a back-supporting strategy achieved through heavy B doping, we fabricated a hybrid honeycomb structure, with an array of UT SiN_x membrane window areas and robust backbone Si support. The SiN_x thickness for a single microchip can be reduced to ~10 nm, which is ~ $^1/_5$ of the commercially used microchips. In addition, these UT microchips have not only superior mechanical integrity but also excellent electron dose stability, demonstrating robust, consistent, and reliable performance.

Thanks to the notable reduction in adverse scattering from thick membranes, the gas cell TEM work based on these UT membranes reveals remarkable improvements in imaging contrast, spatial resolution, and quality of energy dispersive x-ray spectroscopy (EDS) measurements and spectral visibility in EELS. In addition, by using UT microchips, hydrogen charge/discharge dynamics of palladium (Pd) nanoparticles at ambient conditions are demonstrated and studied through detailed quantitative analysis, demonstrating the platform nature of this development and the broad implications with the enhanced spatial resolution and hitherto inaccessible spectral visibility for discriminating important gases (via their nearedge fine structure).

RESULTS

Design and fabrication of the UT SiN_x membrane

Despite the high transparency, a large, freestanding SiN_x membrane window with thicknesses <30 nm lacks physical robustness, which limits experimental reproducibility and thus the mass production of these microdevices. Within gas and liquid TEM experiments, the SiN_x membrane is the only barrier that separates the atmospheric interior from the exterior ultrahigh vacuum (UHV) condition (10^{-8}) to 10⁻⁹ torr). Therefore, the degeneration of mechanical integrity due to stress and dissociation of matter resulting from electron irradiation can lead to catastrophic failure. In experiments, as the membrane is filled with gas or liquid, it can bulge, and the membrane film can be deflected. The smaller Young's modulus (17, 18), which represents the rigidity of the membrane, can result in a larger amount of deflection and higher tendency of membrane rupture. The deflection of membrane is governed by the size, thickness, and other intrinsic properties (i.e., residual stress and Poisson's ratio) of the encapsulation films. A larger window size and thinner window thickness will lead to a larger membrane deflection (19). Therefore, to maintain the physical integrity of the UT SiN_x membrane, the only possible approach is to reduce the membrane size in the planar dimension (20), which means the loss of viewable electron transparent areas. This is especially problematic for the in situ/operando experiments, as it is important to have as wide a field of view as possible to increase the chance of observing the reaction.

To overcome this challenge, we designed the chip to enable placement of multiple small windows over the rigid support. In such a hybrid structure, the surrounding frame would alleviate the mechanical stress, while small and thin membranes could act as electron transparent windows. The calculated amount of membrane

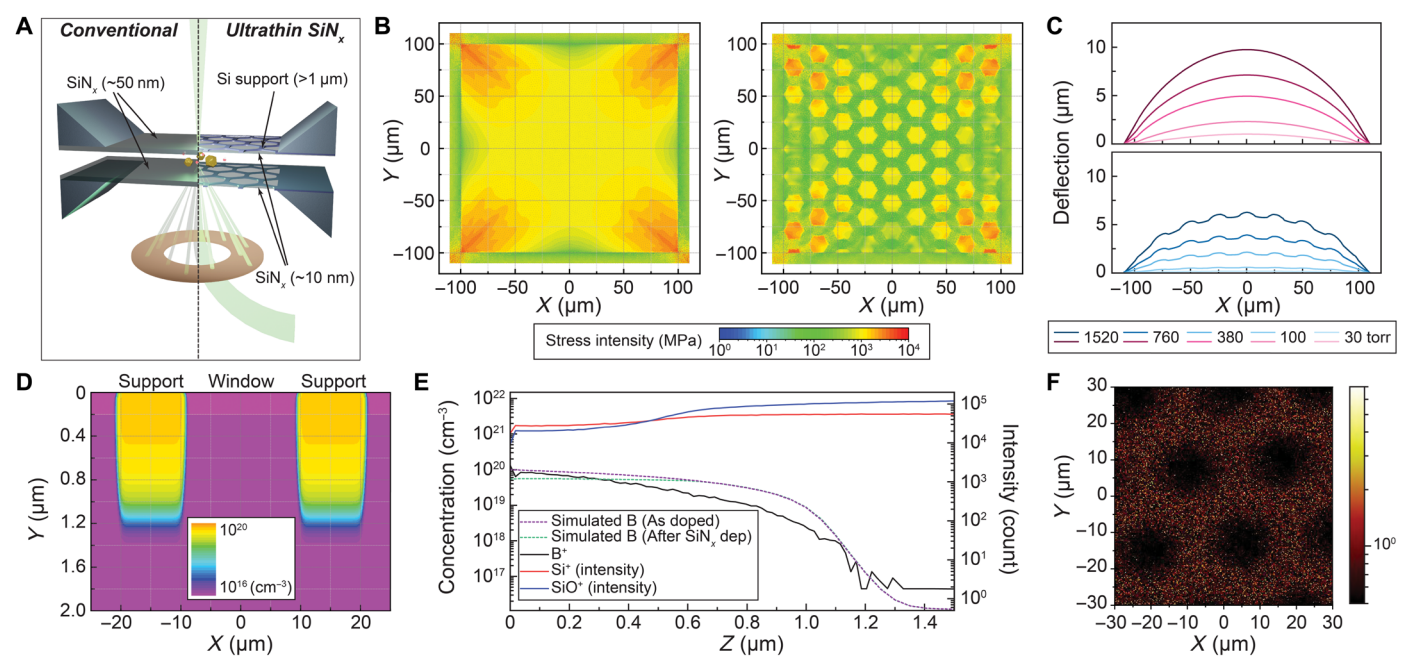


Fig. 1. Structural optimization of the UT SiN_x membrane with a back-supporting structure. (A) Schematic illustration of conventional gas cell TEM and UT gas cell TEM. (B) FEA of stress intensity at a 1-atm pressure gradient for the conventional unsupported SiN_x membrane with a thickness of 50 nm (left) and a UT 10-nm SiN_x membrane with a 1- μ m Si supporting structure (right). The window size is 200 μ m by 200 μ m. (C) Cross-sectional view of the membrane deflection for the unsupported 50-nm SiN_x chip (top) and 10-nm SiN_x chip with a 1- μ m supporting structure (bottom) under various pressure ranges. The window size is 200 μ m by 50 μ m. (D) 2D simulation of dopant boron near the surface of top wafer after diffusion and SiN_x deposition. (E) Dopant profiles of boron and Si. (F) 2D map of dopant boron.

deflection and stress at 1-atm pressure gradient for both conventional and supported UT membrane is shown in Fig. 1 (B and C) and fig. S1. Although the thickness of the SiN_x membrane is reduced to $^1/_5$, the amount of deflection is not increasing but reducing from 13.4 to 10.4 µm in the presence of the back-side silicon (Si) support (movie S1). According to the finite element analysis (FEA) shown in Fig. 1B, the imposed maximum stress is 7.4 GPa for conventional SiN_x membrane with 50-nm thickness at 1-atm pressure gradient. However, the maximum is reduced to 4.4 GPa (movie S2) for our UT membranes with support structure.

Therefore, it can be concluded that the array of the small windows, backed by the rigid Si support, is more resistant to the pressure gradient. Furthermore, simulations based on the parameters of typical liquid cell setup with different membrane structures are compared (Fig. 1C and fig. S1, C and D). It is shown that the amount of membrane deflection at 30 torr of pressure could be as low as ~200 nm for our UT membranes with ~10-nm thickness, which is around $\sim^1/_5$ of conventional cell with ~50-nm thickness and no supporting structure. This implies that the overall thickness of the liquid cell reactor based on this design (~400-nm bulge, 20-nm membranes in total, 50-nm spacer) can be less than 500 nm at the vapor pressure of static aqueous liquid, which means, theoretically, sub-2-Å resolution could be obtained (21).

However, generation of rigid backing supports for the thin membrane is very challenging in terms of conventional fabrication processes. To overcome the processing difficulties, we created the support patterns by taking advantage of the etching rate difference of Si depending on the dopant concentration (22). When the Si is doped with high level of p-type dopants such as boron (B), aluminum (Al), gallium (Ga), and indium (In), a new Fermi level is formed between the valence level and the acceptor level. This makes the space charge layer between Si and the etchant become narrower such that surficial electron recombines easily with excessive holes at the bulk. Therefore, the etching speed is slowed down as the reaction-participating electrons deplete. To differentiate the etching rate of Si, the dopant concentration must exceed 5 × 10¹⁸ atoms cm⁻³, which is a degenerative dopant concentration (0.01 in atomic %).

Process simulations were conducted to verify the feasibility of forming micrometer-thick high-doping region within the Si substrate (Fig. 1D). The final simulated thickness of the degenerated doping region is ~1.04 μ m, while the lateral dopant diffusion is negligible. The time-of-flight secondary ion mass spectroscopy (TOF-SIMS) results on the device also agree well with the simulation with dopant reaching to a depth up to ~1.24 μ m, while ~0.92 μ m depth from surface is doped with degenerative dopant concentration (Fig. 1E). The well-defined doping area acted as supporting frame, and the hexagonal array of undoped membrane areas are visualized in a 2D TOF-SIMS elemental map (Fig. 1F).

The fabrication process of the Si support and UT SiN_x film using the dopant-dependent etch selectivity is illustrated in Fig. 2A and fig. S2. With 10% (v/v) KOH solution at 60°C, the etch rate of intrinsic Si is as high as ~333 nm min⁻¹. However, within ~230 nm of depth below the top surface, the dopant concentration is very high (~5.97 × 10^{19} atoms cm⁻³), and, thus, the etching rate falls to ~17 nm min⁻¹. Last, the dopant concentration is above ~ 10^{20} atoms cm⁻³ near the surface, and the etching rate drops to less than ~1 nm min⁻¹. The etching behavior of the Si is self-limited. Thus, Si within the doped region can be retained as a supporting structure, and

there is a large process window, making this processing physically realizable.

Although the support structure can be further thickened with higher temperature and high-energy ion implant with greater dopant depth, the process conditions listed above are sufficient to achieve a well-defined supporting structure, namely, an average concentration of $\sim 1.21 \times 10^{19}$ atoms cm⁻³ with 1.2- μ m diffusion depth. The released SiN_x membrane with backing support is then etched from the top side using controlled reactive-ion etching (RIE) with the final thickness confirmed by the ellipsometry measurement (fig. S3). The roughness of the SiN_x membrane is maintained with Rq (root mean square roughness) <0.5 nm after etching, which is similar to that of the pristine SiN_x ($R_a \approx 0.63$) (see text SI). Figure 2B shows the variations of optical properties depending on the thickness of remaining SiN_x membrane. The initial ~50-nm SiN_x membrane shows red brown to medium brown color with metallic reflection. As the thickness is further reduced to ~5 nm, the tint of the membranes becomes pale and resembles bare Si substrate. Figure 2C shows the final morphology of the hybrid structure including the hexagonal-shaped electron transparent SiN_x window with a thickness of ~10 nm and heavily doped Si support. The membrane is too transparent to reflect visible light and thus shows the black hole-like contrast in optical image.

Mechanical robustness, resilience, and in situ performance improvement

For the reproducible and practical application of the UT microchip, the structural robustness toward the mechanical and electron beam stresses are prerequisites. The mechanical robustness of the UT $\sin x$ membranes is evaluated with a nano-indentation (fig. S4). The measured fracture toughness of the UT windowed areas is ~13.55 GPa, which is ~3 times of the simulated maximum stress at the 1-atm pressure gradient as shown in Fig. 1B. In addition, by filling the sealed membrane with Ar gas at different pressures, the threshold pressure before the membrane breaks down is measured as high as ~5.3 atm for a 10-nm $\sin x$ membrane (Fig. 2D and movie S3). The devices with a 5-nm thickness start to break at ~1.3 atm, which is still sufficient for the gaseous experiment ranging from UHV to atmospheric pressure.

The dose threshold required to break the membranes with different SiN_x thickness is evaluated using a stationary electron beam (Fig. 2E and fig. S5) in STEM mode. With a relatively high probe current of ~2739 e $^-$ µs $^{-1}$, the average threshold dose is determined to be ~10 10 to 10^{11} e $^-$ Å $^{-2}$ for 10- to 50-nm thickness. For routine atomic resolution STEM imaging and spectrum analysis with a probe current of ~374 e $^-$ µs $^{-1}$, the 10-nm membrane can withstand ~6 min under a stationary electron probe (> 10^{11} e $^-$ Å $^{-2}$) and last indefinitely for a scanning electron probe with a 3-µs dwelling time.

To evaluate the image and signal quality during in situ/operando experimental observations, electron scattering behavior of SiN_x membranes must also be considered. The expected signal-to-noise ratio (SNR) can be quantified for a device of a given thickness (t) by calculating the mean free path (λ_i) (23). The SiN_x has a measured λ_i of ~108.9 nm based on ellipsometry experiments (Fig. 2F and fig. S6). Figure 3A shows analytical calculation of SNR by considering both elastic and inelastic scattering for the total average cross section (9, 19, 24). With a pair of conventional 50-nm SiN_x microchips, the SNR of 10-nm gold and 100-nm carbonaceous materials is less than ~3 and ~5, respectively, at an electron dose of

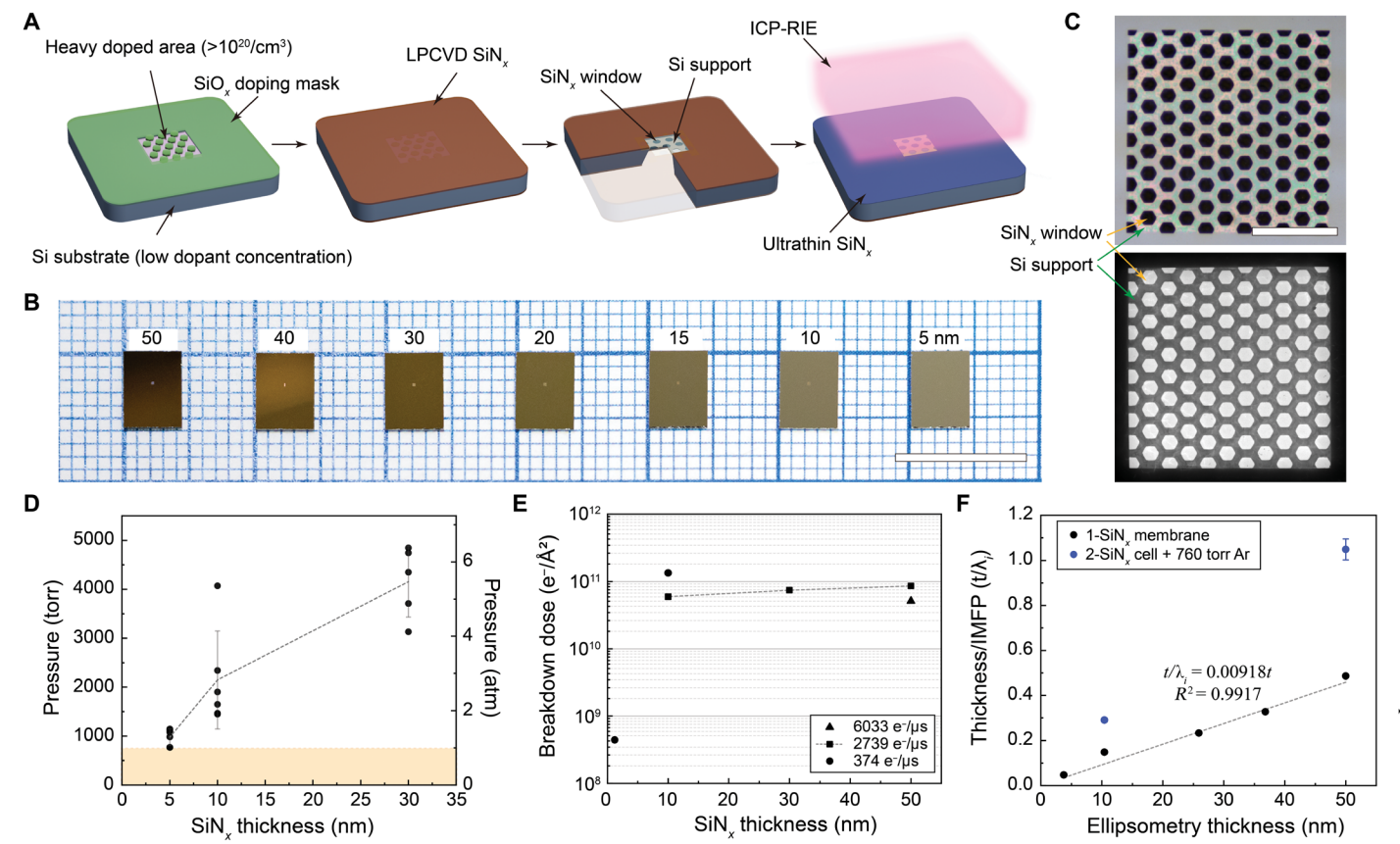


Fig. 2. Fabrication and physical characterizations of the UT SiN_x membrane with a back-supporting structure. (**A**) Fabrication process of the UT SiN_x membranes. (**B**) Digital photograph of fabricated membrane chips with thickness ranging from 50 to 5 nm. Scale bar, 10 mm. (**C**) Optical micrograph (top) and the bright-field TEM image of the UT microchip with honeycomb patterns. The electron transparent area and neighboring Si supporting structure are indicated. Scale bar, 100 μm. (**D**) Pressure resistance of the SiN_x membrane with different thickness. The dashed line indicates the averaged pressure tolerance, and the orange-colored box indicates the general operation pressure. (**E**) Breakdown electron dose of SiN_x membrane under a focused illumination in STEM mode. (**F**) Correlation of membrane thickness and inelastic mean free path (IMFP: t/λ_i) of SiN_x membrane measured with TEM-EELS. The black dots indicate the t/λ_i of single membrane, and blue dots indicate the t/λ_i of assembled closed cells with 760 torr Ar gas.

1000 e⁻ Å⁻². This means that the materials of interest are barely detectable. However, with a pair of 10-nm membranes, an SNR of at least ~3 (Rose criterion) is achievable at ~500 e⁻ Å⁻² for both materials. Figure 3B shows high-resolution TEM (HRTEM) images of 10-nm-thick evaporated Au within the 1-atm Ar-filled gas cell (fig. S7) imaged with an electron dose of ~502 e⁻ Å⁻². In addition, fig. S8 shows HRTEM images based on a single membrane with the same electron dose. The Weber contrast $[(I_s - I_b)/I_b]$ of the image (25) is improved from -0.286 to -0.364 for a single membrane and from -0.165 to -0.281 for a closed gas cell with 1-atm Ar (Fig. 3C). Because of the suppression of background noise, the accessible information limit is greatly improved from ~2.36 to ~1.02 Å based on results from the single face–centered cubic (FCC) gold nanocrystals and ~1.47 to ~1.02 Å from multiple particles (see text SII).

Along with access to high-quality crystallographic information, elemental analysis and electronic structure sensitive valence state analysis of materials can also be acquired with high quality in a UT gas cell TEM experiment. Figure 3D shows the EDS acquired with a 760-torr Ar-filled gas cell having a pair of SiN_x membrane with different thicknesses. The Ar/Si peak ratio is ~0.59 and ~1.00% for the

50- and 30-nm cell, respectively. For the 10-nm gas cell, the ratio is substantially improved to ~8.28%, which is more than 14 times improvement over the conventional setup. While EDS offers rapid and intuitive elemental information, EELS can further provide detailed characteristics such as chemical bonding, band structure, and the valence states of materials. For example, EDS cannot be used to distinguish carbon dioxide (CO2) and carbon monoxide (CO). The different bonding characteristics of two gases are however reflected in both the C-K absorption edge (284 eV) and the O-K absorption edge (532 eV) in the EELS experiment (26) (Fig. 3, E to G). When the UT gas cell is filled with 760-, 380-, and 100-torr gases, we find that CO₂ shows a strong pre-edge "peak" at ~289.6 eV, while CO has a dominant feature at ~285.6 eV, and the CH₄ gas has a dominant peak at ~287.0 eV. In addition, by adopting the UT SiN_x cell, the background intensity is substantially reduced to ~1/4, which makes the peak-to-background (P/B) ratio being improved as high as \sim 5 times for the C-K edge. The signature edge of each gas species is always noticeable from ~100-torr pressure in the UT gas cell. However, because of the substantial background increase from multiple scattering, the signature peak of gas can only be visible with gas pressure larger than ~380 torr for 30- and 50-nm cells.

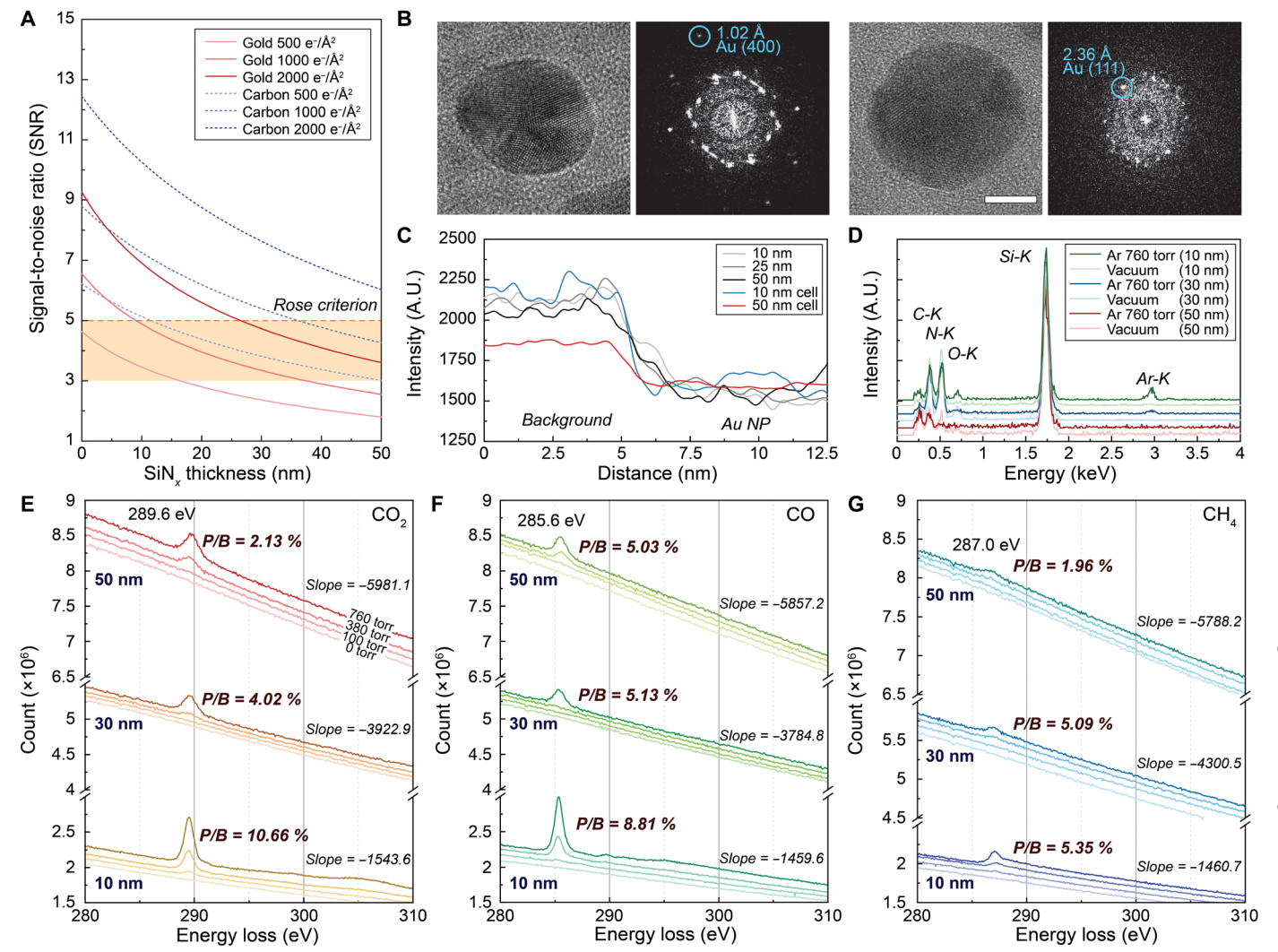


Fig. 3. Improvement on the image and spectroscopic signal quality. (A) Theoretical SNR of 10-nm Au and 100-nm carbonaceous material in closed membranes with 760-torr Ar gas. Values across the x axis indicate the thickness of a single membrane. The orange dashed line indicates Rose criterion (SNR, 5), and the box indicates the SNR region ranging from 3 to 5. (B) HRTEM image and associated fast Fourier transformed patterns of evaporated Au nanoparticles (~10 nm) within a 760-torr Ar gas cell composed of 10-nm (left) and 50-nm (right) SiN $_x$ membranes. The electron dose per image is ~502.0 e $^{-}$ Å $^{-2}$; scale bar, 5 nm. (C) Intensity comparison between the Au nanoparticles and the background under different conditions. (D) EDS of 760-torr Ar gas-filled cell. The Ar/Si peak intensity ratio for 10, 30, and 50 nm cells is ~8.28, ~1.00, ~0.59%, respectively. All the EDS are normalized by using the Si- K_α (1.74 keV) peak. (E to G) C-K edge (284 eV) of CO $_2$, CO, and CH $_4$ gas molecule at different membrane thicknesses. The P/B ratio is calculated by dividing peak area to the baseline area. Exposure per spectra is 0.2 s, and 500 frames are integrated. The used electron dose rate here is ~84.77 e $^{-}$ Å $^{-2}$ s $^{-1}$ A.U., arbitrary units.

Evolution of gas-solid interactions via real-time ED

Beyond superior performance on imaging and chemical analysis, utilization of UT membrane-based microchips also remarkably enhances the retrievable information in reciprocal space. One prototypical example for breakthrough application is to investigate charge/discharge mechanisms in hydrogen storage systems. With the highest energy per mass of any fuel, hydrogen storage is one of the main keys for enabling the technological advancement in stationary power, portable power, and transportation (27, 28). In this context, the ability to directly monitor the dynamic response of material behavior under real conditions is essential for researchers to gain a deep understanding of the underlying charge/discharge mechanisms. The closed-cell in situ/operando technique with our UT microchips is ideal to investigate the hydrogen charge/

discharge dynamics under ambient conditions (room temperature and 760-torr pressure).

Figure 4A shows the selected area ED (SAED) pattern of ~20-nm Pd nanocubes (fig. S9) dispersed on different supporting membranes. As a control, SAED patterns were acquired from nanocubes dispersed on lacey carbon under conventional high-vacuum conditions. Here, the diffraction rings match the expected FCC Pd, and several peaks with planar distances ranging from ~2.26 to ~0.75 Å can be resolved. When the same nanoparticles are instead placed on a conventional SiN_x cells with a thickness of ~50 nm, the additional scattering from the membrane increases the noise floor and hides most of the diffraction peaks other than (200) and (220) reflection. By contrast adjustment, the pattern exposes the low-frequency diffraction ring from (220) to (420), and high-frequency signals [i.e.,

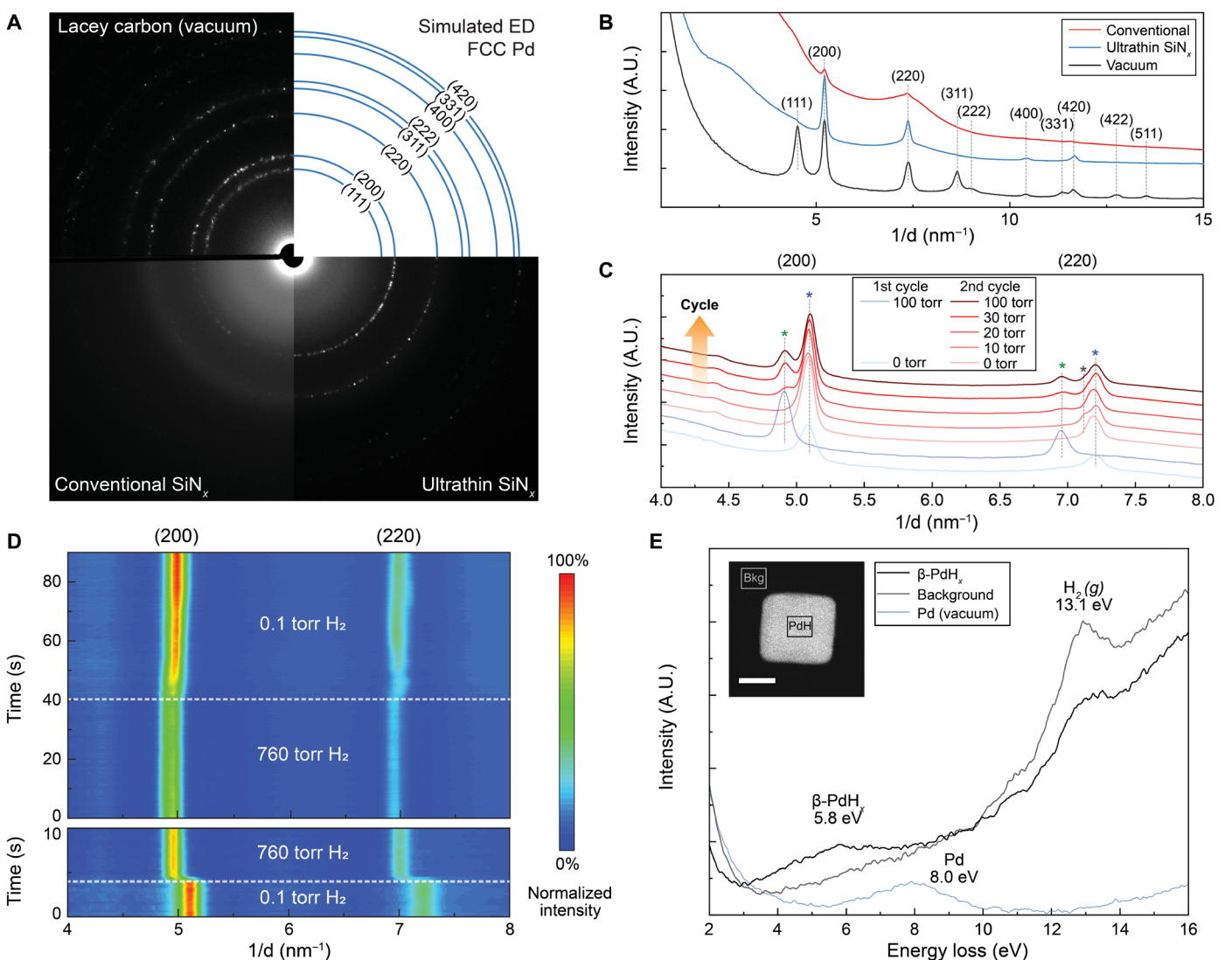


Fig. 4. In situ diffraction of palladium hydride (PdH_x) formation within a UT SiN_x gas cell. (A) SAED of 20-nm FCC Pd nanocubes with different supports. (B) Rotational average of electron diffraction data in (A). (C) Shift of (200) and (220) diffraction peak at different H₂ pressures at the first and second charge cycle. The blue asterisk indicates the Pd peak position, the green asterisk indicates the β-PdH_x, while the gray asterisk at (220) indicates the α-PdH_x. (D) Time evolution of the rotational average of electron diffraction as the H₂ pressure changes. Corresponding real-time movies for the data here are movies S3 and S4. (E) Low-loss EELS of palladium at vacuum, β-PdH_x and the background of the gas cell. Rectangular ROIs for each EELS profile from background and β-PdH_x are labeled in the inset high angle annular dark field (HAADF) image. The scale bar of the inset HAADF image is 10 nm.

(711) and (620)] are nearly invisible. In contrast, experimental data with the UT membrane cell show a notable reduction in background scattering, allowing for observation of rings from ~2.26- to ~0.88-Å spacing without any adjustment (Fig. 4B). By applying the same contrast adjustment, some high-frequency signal up to (711) is practically visible, and (911) is also marginally visible (see text SIII). In situ/operando investigations of these materials at ambient conditions were previously impossible with either x-ray diffraction (XRD) (29) or the E-TEM (30, 31). However, now, both high spatial resolution and faster dynamics could be possible with a UT membrane microchip experiment.

When Pd is exposed to H₂ gas, at the initial stage, molecular H₂ dissociates to H atoms. The H atoms infuse into the interstitial site of Pd lattice and form the β -PdH_x (0.017 < x < 0.65) hydride (32),

resulting in the expansion of lattice parameter. When the UT microchip is filled with more than 100-torr pressure, the lattice parameters of the Pd crystal is expanded by ~4% with expected composition of PdH_{0.62} based on Vegard's law (Fig. 4C) (33). The composition of the hydrogen inside PdH_{0.62} also does not further change within the experimental pressure range (100 to 760 torr) at room temperature. In the initial cycle, 100% of the Pd nanocubes participate in the hydrogenation and dehydrogenation process. However, in the following charge/discharge cycles, we have noticed that a substantial amount (~75%) of the nanocubes become inert to the hydrogen environment and only a portion (~25%) undergoes the phase transition to β -PdH_x, which supports the assertion that nanoparticles with different sizes and morphological features likely display different hydrogen storage behaviors (31).

In addition, it is found that during the second hydrogenation cycles, the lattice expansion coefficient is the same as the initial cycle (~4%), and an intermittent phase equivalent to $\sim \alpha$ -PdH_{0.1} is observed at 10-torr pressure (marked as gray asterisk) and disappears at higher pressure. Moreover, at the charging cycle, the transition between the Pd to β -PdH_x occurs within \sim 0.3 s when the gas cell is filled with 1-atm H₂ (movie S4). Discharging of hydrogen, on the other hand, is slower than the charging cycle, but \sim 75% of β -PdH_x can be reduced to the Pd within \sim 10 s upon the pumping (movie S5 and Fig. 4D).

In comparison, filling the Ar gas from the vacuum does not shift the ED peak positions, indicating that the previous change of lattice parameter is indeed from the hydrogen infusion and not from other factors (movie S6). On the basis of the in situ observations, the calculated diffusion rate of hydrogen $(D = \Delta x^2/2t)$ is ~1.7 × 10⁻¹² cm² s⁻¹ at 1 atm for the Pd (100) crystal plane, which is comparable to the observation from other in situ measurement reported [XRD (29) and E-TEM (30, 31)]. However, the calculated diffusion rate based on this conversion time is substantially lower than that of the bulk observation (34, 35) and molecular dynamics calculations (ranging from $\sim 3.7 \times 10^{-6}$ to $\sim 1.2 \times 10^{-7}$ cm² s⁻¹) (36). Considering the hydrogen molecule dissociation time and that the diffusion rate should remain constant throughout the system, we can conclude that the actual diffusion time within nanoparticle is likely only around 3×10^{-6} s, and most of the ~0.3-s reaction duration is for the adsorption and dissociation of hydrogen, which indicates that the breakdown of the hydrogen molecules to the hydrogen atom is the rate-limiting step at room temperature. Figure 4E is the low loss EELS from the H₂-filled gas cell. The pristine Pd nanocube shows a representative volume plasmon at ~8 eV in the vacuum. However, when the Pd is exposed to 1-atm H₂, another plasmonic excitation appears at ~5.8 eV, which was previously reported as a volume plasmon of β -PdH_x (31). We can also locate the sharp energy loss edge at ~13.1 eV areas across the entire area, which represents the core loss edge of H-K. This observation further supports the formation of β -PdH_x hydride. This in situ demonstration of ED and spectroscopic analysis of Pd charge/discharge mechanism for hydrogen underscores the transformative enhancement in the performance of our UT SiN_x gas cell.

It is readily possible to combine complementary signal detection of EDS and EELS with a potential reaction gas analyzer, which can detect outgoing gas from the whole reaction chamber. With the notable improvement in spatial resolution and spectral visibility, the complete acquisition of mass-based large-molecule analysis, electronic structure and atomic bonding, localization and identity of gaseous species, and zero-delay temporal analysis within both flow and stagnant gas experimental setups are all possible by adopting the UT microchips. We believe that our innovation would open new vistas and provide readily accessible (and widely deployable) setups for mechanistic understanding and insights down to molecular-scale spatial and spectral resolution during fluid-surface interactions.

DISCUSSION

In fluid-surface interactions such as gas-phase catalysis with in situ/operando methods, the major limitation has been the need for thick SiN_x membranes as encapsulated fluidic chips. Herein, we report consistent, reproducible, and scalable fabrication, implementation, and demonstration of a large-area nanoscale reactor based

on UT (\sim <10 nm) SiN $_x$ low-stress membranes. Unlike typical and commercially available thick window chips (with \sim 80- to 100-nm total thickness of SiN $_x$ membrane), our UT window reactors allow for substantially enhanced figures of merit (approaching primary microscope specifications) in imaging resolution, diffraction, and spectral visibility and fidelity.

By adopting these UT microchips into nanoreactor devices, we demonstrate the practical advantages and enhanced in situ/operando performance in uncovering gas-nanoparticle interactions. We show in situ sub-microsecond dynamics in microstructural evolution of β -PdH_x formation at ambient conditions by using in situ/operando ED and EELS. The reduced volume plasmon from encapsulation membranes opens opportunities to monitor important gases through energy loss near-edge structure and low-energy excitations with notable visibility. Collectively, we believe that this is a transformative and "platform" development that would usher a new and expansive era of high spatial- and spectral-resolution measurements in a wide variety of fluid-surface phenomena and readily accessible to researchers to innovate further. In addition, this novel strategy for designing microchips with UT membranes can also be extended to many other places where SiN_x is used as encapsulations and/or support materials, with impact beyond the in situ/operando fields.

MATERIALS AND METHODS

Simulation of membrane deflection and dopant concentration

To assess the membrane deflection for microchips with different supporting structures, FEA was conducted with Ansys 2022R1 mechanical software. To simulate the internal stress after film deposition, SiN_x and the Si wafer were assumed to have zero stress at the initial deposition temperature (835°C). When the patterned structure cooled down to room temperature at furnace, the final freestanding SiN_x membrane has a residual tensile stress of 171.8 \pm 107.4 MPa. The membrane model was then applied with pressure from the top side of the chip, while large deflection mode was enabled. The z-directional displacement of node and stress intensity were then plotted to show the deflection and membrane stress.

The doping profiles were simulated using the Silvaco Technology Computer Aided Design software. The mesh grid setting is 50 nm \times 50 nm near the doping boundaries. The background dopant concentration of Si substrate is 10^{16} atoms cm⁻³ (n-type). For dopant diffusion, Fick's Second Law was applied to the experimental parameters including the intrinsic properties of the Si (100) plane, diffusion coefficient of boron, and the solid-solubility limit of B in Si. Boron atoms from a solid source were first diffused into the original Si wafer creating an original dopant concentration of 10^{16} atoms cm⁻³ after heating at 1000° C for 3 hours. After doping, the wafer was then heated and kept at 835° C for 16 min, which was the deposition conditions for SiN $_x$ film with 50-nm thickness to subsume the extra diffusion caused by the elevated temperature during SiN $_x$.

Fabrication of UT SiN_x chips

Prime grade B-doped 4-inch double side polished (DSP) wafers (resistivity: 1 to 20 ohm·cm) with a thickness of 300 µm were purchased from University Wafer (Boston, MA). The actual resistivity of the used wafer was 1.59 ohm·cm based on Hall effect measurement. The



wafers were first cleaned with freshly prepared piranha solution (three parts of concentrated H₂SO₄ and one part of 30% H₂O₂) to remove any absorbed particles and organic contaminants. By further cleaning with 49% hydrofluoric acid (HF), the native oxide layer formed in the previous step was removed. To create localized highdoping areas with lower etch rate, a SiO_x dopant mask was first created. Wet silicon oxide with a thickness of 400 nm was deposited by using the Tystar Tytan furnace. Then, the AZ 4620-positive photoresist was coated on the oxide wafer. The mask pattern was created using Heidelberg MLA150 maskless aligner and further developed with AZ 400 K. The exposed oxide pattern was then removed with HF bath. With the abovementioned cleaning process, photoresist was removed. Subsequently, the clean pattern-created wafer was doped using BN-1250 planar solid boron source from Saint-Gobain Ceramics (Paris, France) for 3 hours at 1000°C. During the doping process, B atoms diffused into both exposed Si and masking SiO_x areas, but the SiO_x area was later removed with 49% (w/w) HF before depositing the SiN_x membrane. A total of 50 nm of low-stress SiN_x was then deposited by using the chemical vapor deposition method with dichlorosilane (SiH2Cl2) and ammonia (NH3) gaseous precursor at 835°C. The SiN_x at the opposite undoped surface was partially opened with a Samco RIE-10NR (Tokyo, Japan) ion coupled plasmareactive ion etch (ICP-RIE) device to initiate the etching of undoped silicon. The wafer was then dipped to 10% (w/w) potassium hydroxide (KOH) solution at 60°C for wet etch. To maintain the concentration of KOH solution, a small amount of isopropyl alcohol was added above the meniscus. The wafer was then retrieved and diced into the desired dimension. Last, the thickness (ranging from ~50 to ~5 nm) of the suspended SiN_x membrane was achieved by varying the ICP-RIE etching time. The membrane thickness was determined by the ellipsometry measurement.

Physical assessments of the UT chips

The non-interlaced mode of an M6 TOF SIMS (ION-TOF GmbH, Muenster, Germany) was used to conduct SIMS depth profiling analysis. Sputtering was carried out on a 300 by 300 μm² square area using 2-keV oxygen ions, which were directed at a 45° angle to the surface normal of the sample. For the analysis, pulsed 30-keV Bi ions were used and rastered over a 65 by 65 μ m² square area at a 45° angle to the surface normal. The analyzer was positioned normally to the sample surface, and the analysis area was situated in the center of the sputtered area. The depth of the crater was measured using a stylus profilometer (Bruker Dektak 150) and calibrated accordingly. The SIMS intensity of the boron was calibrated by using the averaged carrier concentration obtained from the Hall effect measurement. The conductivity and the carrier concentration of the uniformly doped boron chip was measured with the Van der Pauw method using Lake Shore Cryotronics HMS 8404 (Westerville, OH). The thickness of the SiN_x membrane was measured with a variable-angle spectroscopic ellipsometry using J.A. Woollam M2000U and alpha-SE Ellipsometer (Lincoln, NE).

The nanomechanical testing was performed on the Bruker TI 950 TriboIndenter equipped with a three-side pyramid diamond indenter tip (Berkovich). The indentations were conducted under the load-controlled mode consisting of three segments (loading, holding for 2 s and unloading in 5 s). A typical loading-displacement curve was acquired from multiple areas of membranes with different thickness. The maximum load $P_{\rm max}$, maximum depth $h_{\rm max}$, final depth after unloading $h_{\rm r}$, and the slope of the upper portion of the unloading curve

S were monitored in a full loading-unloading cycle. The material properties, such as reduced elastic modulus and hardness, could be extracted by analyzing the data with the method developed by Pharr and Oliver (37). Pressure stability of the closed cell was tested with a homemade apparatus, which is described elsewhere (10). The real-time movie and the applied pressure were recorded individually and synchronized afterward. The pressures at the moment of the breaking were surveyed. Electron beam stability of the SiN_x cell was tested by focusing electron probe with different intensities onto the membrane directly until it reached the breaking point.

Gas cell TEM

For the model system, the 20-nm Pd nanocubes were used for our gas cell experiments. The synthesis methods for these nanoparticles were described in detail in previous reports (38). Gas environmental cell TEM was conducted using Protochips Atmosphere 210 System (Morrisville, NC). The system consists of a gas-supplying manifold system and a specimen rod, which holds two windowed microchips for encapsulation. The gas supply system can supply experimental gas up to 1 atm of pressure, either in static or flow configuration. The pressure of the gas cell is probed with two in-line gauges at the inlet and outlet side of holder. There is a negligible amount of flow resistance along the flow path and pressure value probed at two points were synchronized immediately upon the gas flow. Therefore, the internal pressure of the gas cell is considered to be the same as the probing points. The pressure value indicated in Figs. 3 (B and D to G) and 4 (C to E) is the set pressure value, which differs less than ~2% from the actual value for clear visualization and comparison between the experiments (see text SIV). The fabricated UT SiN_x chips were cleaned with oxygen plasma and placed into the specimen rod, with the membrane sides facing each other. The suspension of Pd nanocube was drop-casted on the top membrane chip and dried. Between the stacked chips, a chemically inert fluoroelastomer gasket was placed to seal the internal environment from outside. The assembled gas cell within the specimen rod was then inserted to the microscope and the internal loop was purged with ultrahigh-purity Ar gas. The desired gas was then flown into the environmental cell and purged at least three cycles between each experiment.

All S/TEM and EELS characterizations were conducted on JEOL ARM 200CF TEM (Japan), which was operated at 200 keV. This microscope was equipped with a probe corrector, a Gatan OneView camera, and a Quantum EEL spectrometer. The spectrometer was updated with a K2 Summit direct electron detector. The low loss data were collected using the USC 1000 GIF camera, and the core loss data were collected using the K2 direct detector. The used GIF entrance aperture and energy dispersion were 2.5 mm and 0.1 eV per channel, respectively. The collection angle for spectrum mapping was from 0 to 70 mrad.

Supplementary Materials

This PDF file includes:

Figs. S1 to S15 Texts S1 to S4 Table S1 Legends for movies S1 to S6

Other Supplementary Material for this manuscript includes the following:

REFERENCES AND NOTES

- L. Luo, B. Liu, S. Song, W. Xu, J.-G. Zhang, C. Wang, Revealing the reaction mechanisms of Li-O₂ batteries using environmental transmission electron microscopy. *Nat. Nanotechnol.* 12, 535-539 (2017).
- J. M. Yuk, J. Park, P. Ercius, K. Kim, D. J. Hellebusch, M. F. Crommie, J. Y. Lee, A. Zettl, A. P. Alivisatos, High-resolution EM of colloidal nanocrystal growth using graphene liquid cells. Science 336, 61–64 (2012).
- N. D. Loh, S. Sen, M. Bosman, S. F. Tan, J. Zhong, C. A. Nijhuis, P. Král, P. Matsudaira, U. Mirsaidov, Multistep nucleation of nanocrystals in aqueous solution. *Nat. Chem.* 9, 77–87 (2017)
- R. E. Schreiber, L. Houben, S. G. Wolf, G. Leitus, Z.-L. Lang, J. J. Carbo, J. M. Poblet, R. Neumann, Real-time molecular scale observation of crystal formation. *Nat. Chem.* 9, 369–373 (2017).
- J. S. Du, K. He, Y. Xu, C. B. Wahl, D. D. Xu, V. P. Dravid, C. A. Mirkin, Galvanic transformation dynamics in heterostructured nanoparticles. Adv. Funct. Mater. 31, 2105866 (2021).
- B. Song, Y. Yang, M. Rabbani, T. T. Yang, K. He, X. Hu, Y. Yuan, P. Ghildiyal, V. P. Dravid, M. R. Zachariah, W. A. Saidi, Y. Liu, R. Shahbazian-Yassar, *In situ* oxidation studies of high-entropy alloy nanoparticles. *ACS Nano* 14, 15131–15143 (2020).
- K. He, K. Kim, C. J. Villa, S. M. Ribet, P. Smeets, R. Dos Reis, P. W. Voorhees, X. Hu, V. P. Dravid, Degeneration behavior of Cu nanowires under carbon dioxide environment: An in situ/ operando study. Nano Lett. 21, 6813–6819 (2021).
- E. Kennedy, E. M. Nelson, T. Tanaka, J. Damiano, G. Timp, Live bacterial physiology visualized with 5 nm resolution using scanning transmission electron microscopy. ACS Nano 10, 2669–2677 (2016).
- N. de Jonge, D. B. Peckys, G. Kremers, D. Piston, Electron microscopy of whole cells in liquid with nanometer resolution. Proc. Natl. Acad. Sci. U. S. A. 106, 2159–2164 (2009).
- K. Koo, J. Park, S. Ji, S. Toleukhanova, J. M. Yuk, Liquid-flowing graphene chip-based high-resolution electron microscopy, Adv. Mater. 33, e2005468 (2021).
- G. Dunn, V. P. Adiga, T. Pham, C. Bryant, D. J. Horton-Bailey, J. N. Belling, B. L. France, J. A. Jackson, H. R. Barzegar, J. M. Yuk, S. Aloni, M. F. Crommie, A. Zettl, Graphene-sealed flow cells for *in situ* transmission electron microscopy of liquid samples. *ACS Nano* 14, 9637–9643 (2020).
- K.-L. Liu, C.-C. Wu, Y.-J. Huang, H.-L. Peng, H.-Y. Chang, P. Chang, L. Hsu, T.-R. Yew, Novel microchip for in situ TEM imaging of living organisms and bio-reactions in aqueous conditions. *Lab Chip* 8, 1915–1921 (2008).
- J. Yang, M. K. Choi, Y. Sheng, J. Jung, K. Bustillo, T. Chen, S.-W. Lee, P. Ercius, J. H. Kim, J. H. Warner, E. M. Chan, H. Zheng, MoS₂ liquid cell electron microscopy through clean and fast polymer-free MoS₂ transfer. *Nano Lett.* 19, 1788–1795 (2019).
- K. Koo, S. M. Ribet, C. Zhang, P. J. Smeets, R. Dos Reis, X. Hu, V. P. Dravid, Effects of the encapsulation membrane in *operando* scanning transmission electron microscopy. *Nano Lett.* 22, 4137–4144 (2022).
- C. Ophus, Four-dimensional scanning transmission electron microscopy (4D-STEM): From scanning nanodiffraction to ptychography and beyond. *Microsc. Microanal.* 25, 563–582 (2019).
- S. M. Ribet, A. A. Murthy, E. W. Roth, R. Dos Reis, V. P. Dravid, Making the most of your electrons: Challenges and opportunities in characterizing hybrid interfaces with STEM. *Mater. Today* 50, 100–115 (2021).
- K. Babaei Gavan, H. J. Westra, E. W. van der Drift, W. J. Venstra, H. S. van der Zant, Size-dependent effective Young's modulus of silicon nitride cantilevers. *Appl. Phys. Lett.* 94, 233108 (2009).
- X.-J. Xu, Z.-C. Deng, B. Wang, Closed solutions for the electromechanical bending and vibration of thick piezoelectric nanobeams with surface effects. J. Phys. D Appl. Phys. 46, 405302 (2013).
- M. Li, R. Knibbe, A study of membrane impact on spatial resolution of liquid in situ transmission electron microscope. Microsc. Microanal. 26, 126–133 (2020).
- J. Vlassak, W. Nix, A new bulge test technique for the determination of Young's modulus and Poisson's ratio of thin films. J. Mater. Res. 7, 3242–3249 (1992).
- N. De Jonge, F. M. Ross, Electron microscopy of specimens in liquid. Nat. Nanotechnol. 6, 695–704 (2011).
- H. Seidel, L. Csepregi, A. Heuberger, H. Baumgärtel, Anisotropic etching of crystalline silicon in alkaline solutions: I. orientation dependence and behavior of passivation layers. J. Electrochem. Soc. 137, 3612–3626 (1990).

- R. F. Egerton, in Electron Energy-loss Spectroscopy in the Electron Microscope (Springer Science & Business Media, 2011), pp. 294–295.
- L. Reimer, Transmission Electron Microscopy: Physics of Image Formation and Microanalysis (Springer, 2013), vol. 36.
- Y. Zhu, N. D. Browning, The role of gas in determining image quality and resolution during in situ scanning transmission electron microscopy experiments. ChemCatChem 9, 3478–3485 (2017).
- C. Ahn, O. L. Krivanek, EELS Atlas: A Reference Guide of Electron Enery Loss Spectra Covering All Stable Elements (Joint project of the ASU HREM facility and GATAN, 1983).
- B. D. Adams, A. Chen, The role of palladium in a hydrogen economy. *Mater. Today* 14, 282–289 (2011).
- G. W. Crabtree, M. S. Dresselhaus, M. V. Buchanan, The hydrogen economy. *Phys. Today* 57, 39–44 (2004).
- N. J. Johnson, B. Lam, B. P. MacLeod, R. S. Sherbo, M. Moreno-Gonzalez, D. K. Fork,
 C. P. Berlinguette, Facets and vertices regulate hydrogen uptake and release in palladium nanocrystals. *Nat. Mater.* 18, 454–458 (2019).
- A. Baldi, T. C. Narayan, A. L. Koh, J. A. Dionne, In situ detection of hydrogen-induced phase transitions in individual palladium nanocrystals. *Nat. Mater.* 13, 1143–1148 (2014).
- T. C. Narayan, F. Hayee, A. Baldi, A. Leen Koh, R. Sinclair, J. A. Dionne, Direct visualization of hydrogen absorption dynamics in individual palladium nanoparticles. *Nat. Commun.* 8, 14020 (2017).
- F. Manchester, A. San-Martin, J. Pitre, The H-Pd (hydrogen-palladium) system. J Phase Equilib. 15, 62–83 (1994).
- J. M. Polfus, T. Peters, R. Bredesen, O. M. Løvvik, Vacancy diffusion in palladium hydrides. Phys. Chem. Chem. Phys. 23, 13680–13686 (2021).
- M. Beg, D. Ross, The quasielastic scattering of cold neutrons from the beta phase of palladium hydride (and hydrogen diffusion). J. Phys. C Solid State Phys. 3, 2487–2500 (1970).
- P. Davis, E. Seymour, D. Zamir, W. D. Williams, R. Cotts, Nuclear magnetic resonance study of hydrogen diffusion in palladium-silver alloys. J. Less Common Met. 49, 159–168 (1976).
- X. Zhou, T. W. Heo, B. C. Wood, V. Stavila, S. Kang, M. D. Allendorf, Temperature-and concentration-dependent hydrogen diffusivity in palladium from statistically-averaged molecular dynamics simulations. *Scr. Mater.* 149, 103–107 (2018).
- G. Pharr, W. Oliver, Measurement of thin film mechanical properties using nanoindentation. MRS Bull. 17, 28–33 (1992).
- M. Jin, H. Liu, H. Zhang, Z. Xie, J. Liu, Y. Xia, Synthesis of Pd nanocrystals enclosed by {100} facets and with sizes <10 nm for application in CO oxidation. Nano Res. 4, 83–91 (2011).

Acknowledgments: This work made use of the EPIC, Keck-II, SPID, and NUFAB facility of Northwestern University's NUANCE Center. S.M.R. acknowledges support from the IIN Ryan Fellowship and the 3M Northwestern Graduate Research Fellowship. Funding: This work was supported by the following: ARO MURI program W911NF-18-1-0200 (V.P.D.), Air Force Office of Scientific Research FA9550-22-1-0300 (V.P.D., K.K., and R.d.R.), National Research Foundation of Korea (NRF) Basic Science Research Program grant 2022R1A6A3A03059199 (K.K.), National Research Foundation of Korea (NRF) grant funded by the Korea government (MSIT) NRF-2022R1A2C2008929 (J.P. and J.M.Y.), Soft and Hybrid Nanotechnology Experimental (SHyNE) Resource NSF ECCS-2025633 (V.P.D.), International Institute of Nanotechnology, and Northwestern's MRSEC program NSF DMR-2308691. Author contributions: Conceptualization: V.P.D., X.H., K.K., R.d.R., Y.L., P.J.M.S., and J.M.Y. Methodology and analysis: K.K., V.P.D., Z.L., Y.L., X.C., G.S., X.F., R.d.R., Y.J., X.H., and J.M.Y. Supervision: X.H., V.P.D., G.S., Z.L., and J.M.Y. Writingoriginal draft: V.P.D., X.H., K.K., S.M.R., Y.L., P.J.M.S., and Z.L. Writing—review and editing: S.M.R., Y.L., J.P., J.M.Y., X.H., V.P.D., K.K., X.C., and Z.L. Competing interests: K.K., X.H., and V.P.D. are inventors on U.S. provisional patent no. 63413097, filed by Northwestern University. All other authors declare that they have no competing interests. Data and materials availability: All data needed to evaluate the conclusions in the paper are present in the paper and/or the Supplementary Materials. The materials can be provided by V.P.D. pending scientific review and a completed material transfer agreement. Requests for the materials should be submitted

Submitted 7 July 2023 Accepted 18 December 2023 Published 17 January 2024 10.1126/sciadv.adj6417